ROYAL SOCIETY
OF CHEMISTRY

PAPER

CrossMark
click for updates

A mesoporous–planar hybrid architecture of methylammonium lead iodide perovskite based solar cells†

Ravi K. Misra,[a] Sigalit Aharon,[a] Michael Layani,[b] Shlomo Magdassi[a] and Lioz Etgar*[a]

We report a hybrid mesoporous–planar architecture of methylammonium lead iodide perovskite based solar cells, to combine the benefits of both the mesoporous and planar architectures in a single device. A mesoporous-TiO$_2$ grid was fabricated on a compact TiO$_2$ layer, through a self-assembly process based on directional wetting, providing regions with and without mesoporous-TiO$_2$, followed by perovskite deposition and back contact evaporation (hybrid cells). The hybrid cells showed up to 10.7% power conversion efficiency (PCE) as compared to 13.5% and 6.3% for their mesoporous and planar counterparts, respectively. Interestingly, the hybrid cells are found to show a short circuit current density (J_{sc}) as high as the J_{sc} of the mesoporous TiO$_2$ based cells and proved to conserve the current density even in the absence of mesoporous-TiO$_2$ from planar parts of the hybrid cells. The cells showed the best fill factor as compared to their mesoporous and planar counterparts. The areal variation in the meso to planar ratio has also been realized by changing the grid size to demonstrate the effect of the architecture on the cell performance. Charge extraction measurements have been used to obtain insight into the recombination inside different solar cells architectures. The hybrid cell structure emerged as a novel promising design for perovskite solar cells.

Introduction

Perovskite solar cells (PSCs) have seen tremendous development in the past few years since their first report as a visible light sensitizer in 2009 (ref. 1) and recently achieved a record high power conversion efficiency (PCE) of 22.1%.[2] The highest efficiency PSCs published so far and available in the public domain are the triple cation based perovskite cells with 21.1% efficiency.[3] Simple synthesis and good optical and electronic properties, in addition to low cost,[4–6] make these inorganic–organic hybrid perovskites the material of choice for the PV community. Two architectures of PSCs introduced so far are namely, mesoporous (meso) and planar devices.[5] A typical mesoporous architecture has a meso-TiO$_2$ layer, serving as a porous support for the deposited perovskite layer and its infiltration. Interestingly, all the PSCs with 20+% efficiency are essentially based on mesoporous device architectures,[2,3,7] making the mesoporous architecture the preferable one, despite the fact that the exact role of meso-TiO$_2$ in these cells is yet to be well established.[8–10] Contrary to the very good PCE, the

phenomenon of hysteresis is quite common in this architecture. On the other hand, planar devices, which can be fabricated by the direct deposition of a perovskite layer on compact titania, which are lacking the meso-TiO$_2$, are even more simple to realize.[11–15] The PSCs with a planar architecture are found to show significant PCE, though the meso-TiO$_2$ layer is absent in this cell structure.[11–18] This makes them popular, as they have a lower fabrication cost and avoid the TiO$_2$ sintering step at high temperatures. Planar cells with flat and inverted structures using organic electron/hole transporting materials (ETMs/HTMs) have shown negligible hysteresis.[16–18]

This motivated us to evaluate the combination of the mesoporous and planar architectures in a single cell, not only combining the benefits of both the architectures but also providing an intermediate architecture for the detailed study of the behavior of meso-TiO$_2$ in a PSC. This architecture of meso–planar hybrid PSCs was achieved by a directional self-assembly of the TiO$_2$ nanoparticle layer, in the form of a grid.

In this work, we demonstrate for the first time an architecture of PSCs, which has both the planar and mesoporous parts in a single cell (e.g. meso–planar hybrid architecture of PSCs). The morphological characterization of the meso–planar hybrid layer and the fabricated cells was performed by using High Resolution Scanning Electron Microscopy (HR-SEM) and optical microscopy. The photovoltaic performance of these cells has also been compared with traditional meso and planar architectures. The areal ratio of meso/planar has been varied in order

[a]Institute of Chemistry, Casali Center for Applied Chemistry, Hebrew University of Jerusalem, Israel-91904. E-mail: lioz.etgar@mail.huji.ac.il

[b]School of Materials Science and Engineering, Nanyang Technological University, 50 Nanyang Avenue, Singapore 639798

to see the trend in performance with decreasing meso-component in the cells. The charge extraction measurements were used to analyze the electronic properties of the hybrid architecture cells and compare them with meso and planar counterparts. The meso–planar hybrid cells provide a tool to compare the electronic properties of different architectures and to study the effect of the presence or absence of meso-TiO_2 on the photovoltaic parameters of the cells.

Experimental

Synthesis of precursors

Synthesis of methyl ammonium iodide (MAI) was done by reacting 27.8 mL of methylamine (40% in methanol, TCI) with 30 mL of hydroiodic acid (57 wt% in water, Aldrich) in a 250 mL round bottom flask at 0 °C for 2 h with stirring. The solvent was removed using a rotary evaporator at 50 °C for 1 h and the precipitate was collected. This precipitate was washed with ethanol by stirring for 30 minutes. The collected mixture was filtered and washed with diethylether repeatedly for three times and the white solid was collected and dried at 60 °C in a vacuum oven for 24 h.

Fabrication of devices

Fluorine doped tin oxide coated SnO_2:F (FTO) conducting glass (15, Pilkington) substrates have been cut in the desired size and etched with Zn/HCl followed by extensive cleaning. A hole blocking layer was then deposited on the conducting side of the glass using a solution of titanium diisopropoxide bis(acetylacetonate) (TiDIP, 75% in isopropanol, Aldrich) in ethanol using spin coating followed by annealing at 450 °C for 30 minutes. Another blocking layer is deposited only on the set of planar cells to achieve the desired thickness.

Then the mesoporous titania layer was deposited on the blocking layer in different ways in mesoporous and meso–planar hybrid cells according to their architecture. In order to perform the deposition of the mesoporous layer on meso-cells, TiO_2 paste (Dyesol, DSL-90T TiO_2 NP paste) was diluted in ethanol (dilution of 0.1 g of the paste in 0.32 g of ethanol absolute), then spin coated on top of the compact TiO_2 layer and annealed at 500 °C for 30 minutes. The self-assembly of meso-TiO_2 in the form of a grid has been achieved using a previously reported technique, while using a metallic mesh of 50 and 72 micron openings. The process of fabrication of a transparent grid was reported elsewhere in the context of preparing transparent conductive coatings.[19–22] In this research, a screen printing stainless steel mesh (Ponger 2000 Israel) was placed onto the mesoporous TiO_2 layer which is placed in a closed box with a humidity of 30–40% RH, and ~20 °C. Prior to the placement, the mesh is hydrophilized by plasma cleaning (in 20% oxygen for 2 minutes, PICO system, Deiner electronics) in order to enable wetting and movement of the liquid towards the wires of the mesh. In a typical deposition step, the TiO_2 paste (Dysol, DSL-90T) has been diluted in ethanol (0.1 g in 64 g of absolute ethanol). The compact BL deposited substrates were placed on a flat surface under controlled humidity conditions. The mesh was placed on the substrate in a way that mesh wires are touching the surface without strain. A 7 micro liter solution was dropped on the mesh and allowed to dry for 30 minutes. The as prepared grid was carefully separated from the mesh and put for annealing at 500 °C for 30 minutes through different ramp steps. All three architectures were then treated with $TiCl_4$ for 30 minutes at 70 °C and washed, followed by annealing at 500 °C for 30 minutes.

A two-step method for perovskite deposition has been used for all three architectures. In the first step, 1 M solution of PbI_2 in the DMF : DMSO mixture (85 : 15 ratio) was spin coated on the already prepared photoelectrodes, followed by annealing for 45 min at 70 °C. The PbI_2 coated film was then removed from the hot plate, cooled for a while and dipped in a 10 mg mL^{-1} solution of methylammonium iodide (MAI), in isopropanol for 30 seconds, resulting in the formation of dense black-brown $MAPbI_3$. The cells were annealed at 90 °C for another 30 min. The hole transporting layer of spiro-OMeTAD was deposited by spin coating 40 μL of the following described solution (4000 rpm, 30 s). The solution was prepared by dissolving 72.3 mg of 2,2′,7,7′-tetrakis-(N,N-di-4-methoxyphenylamino)-9,9′-spirofluorine (spiro-OMeTAD) in 1 mL chlorobenzene. 26.3 μL of the bis(trifluoromethane)sulfonimide lithium salt in acetonitrile (520 mg mL^{-1}), 29 μL of tris(2-(1H-pyrazol-1-yl)-4-$tert$-butylpyridine)-cobalt(III) tris(bis(trifluoromethylsulfonyl)imide) in acetonitrile (300 mg mL^{-1}) and 19.2 μL of 4-$tert$-butylpyridine were added to the spiro-OMeTAD solution as additives. Then, the back contact was deposited by evaporating 70 nm of gold under a pressure of 5×10^{-6} Torr. The active area was 0.09 cm^2.

Finally, encapsulation of these cells was done inside the glovebox using a DuPont™ Surlyn® film as a spacer and sticker for the upper glass by melting it with the help of a welding-pen.

Photovoltaic characterization

Photovoltaic measurements were made on a New Port system, composed of an Oriel I–V test station using an Oriel Sol3A simulator. The solar simulator was class AAA for its spectral performance, uniformity of irradiance, and temporal stability. The solar simulator was equipped with a 450 W xenon lamp. The output power was adjusted to match AM 1.5 global sunlight (100 mW cm^{-2}). The spectral match classifications were IEC60904-9 2007, JIC C 8912, and ASTM E927-05. I–V curves were obtained by applying an external bias to the cell and measuring the generated photocurrent with a Keithley model 2400 digital source meter. The voltage step and delay time of the photocurrent were 10 mV and 40 ms, respectively.

Morphological characterization

The grids were observed by using an optical microscope (MRC Israel). Ultra-high resolution scanning electron microscopy (UHR-SEM) was performed by using a Sirion UHR SEM (FEI, Field Emission Instruments), The Netherlands. The measurement conditions were 5 kV at various magnifications.

Charge extraction measurements

Charge extraction measurements were done using a Autolab potentiostat–galvanostat (PGSTAT) with a FRA32M LED driver equipped with a white light source. The cells were illuminated from the substrate side. Nova 1.11 software program was used to collect and analyse the data obtained. A typical charge extraction experiment composed of (1) a two-second step in which the cell is discharged in the dark; (2) the cell is then disconnected and illuminated for 2 seconds (illumination time); (3) the light is then switched off and the system waits for a certain time called the delay time. In this step a charge recombination occurs inside the cell; (4) the cell is reconnected and the charges which were left and didn't recombine are extracted and measured. This process is being repeated for different delay times, from 0.5 seconds to 15 seconds. The charges collected were plotted against the delay time to give insight into the life-span of the charges after a certain delay time.

Results and discussion

Cell architecture and morphology

Fig. 1 shows a schematic illustration of the different architectures, the mesoporous, the planar and the meso–planar hybrid PSCs.

The deposition of the meso-TiO$_2$ grid to provide the base for the meso–planar hybrid structure is based on self-assembly of the TiO$_2$ nanoparticles (NPs) to form a grid. Titania's self-assembly took place along the mesh-walls, making the junction points a hill, and centers of the mesh a valley without the presence of meso-titania. The mesh assisted grid deposition was demonstrated already by our group for semitransparent perovskite solar cells and in previous work on a silver grid by our group and transparent conducting grid deposition by Higashitani et al.[19–22] The grid formation in the present study was performed by using a metallic mesh with mesh sizes of 50 and 72 μm. Following the formation of the meso-TiO$_2$ grid, a methyl ammonium lead iodide (MAPbI$_3$) perovskite layer was deposited using the two-step process, followed by deposition of 2,2′,7,7′-tetrakis-(N,N-di-4-methoxyphenylamino)-9,9′-spirofluorine (spiro-OMeTAD), the hole transporting material (HTM), before deposition of the back contact. The hybrid meso–planar cells have areas with and without mesoporous TiO$_2$, which enables them to work as a hybrid between the mesoporous and planar architectures of PSCs.

Fig. 2a and b show the optical images of the self-assembled meso-TiO$_2$ grid (with 50 micron mesh opening) and a complete meso–planar hybrid perovskite solar cell from a top view. It can be seen from Fig. 2a that self-assembly preferably takes place along the wires of the mesh, due to the capillary forces and the coffee ring effect. Fig. 2b shows the TiO$_2$ grid and the perovskite film on top of it; the dense perovskite coverage can be seen in the form of circles with dark color, whereas the area with the lighter part of the image shows the least perovskite covered parts.

The top view of the same grid under High Resolution Scanning Electron Microscopy (HR-SEM) is presented in Fig. 2c. The higher density of TiO$_2$ along with the mesh wires can be seen as
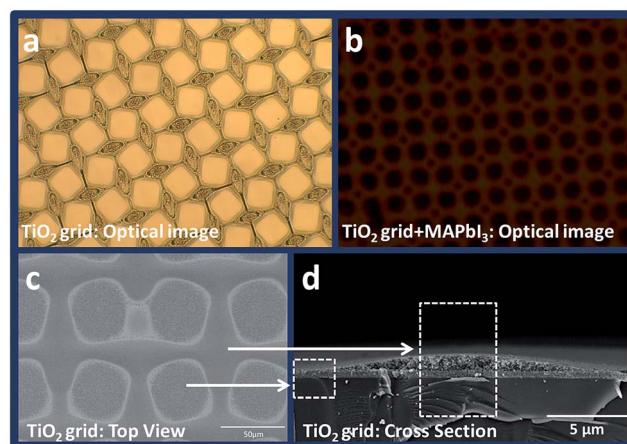

Fig. 2 Optical image of (a) the mesoporous-titania grid deposited with the help of a mesh (mesh size 50 micron) and (b) perovskite deposited on the TiO$_2$ grid; (c) top view SEM image and (d) the cross sectional SEM image of the grid.
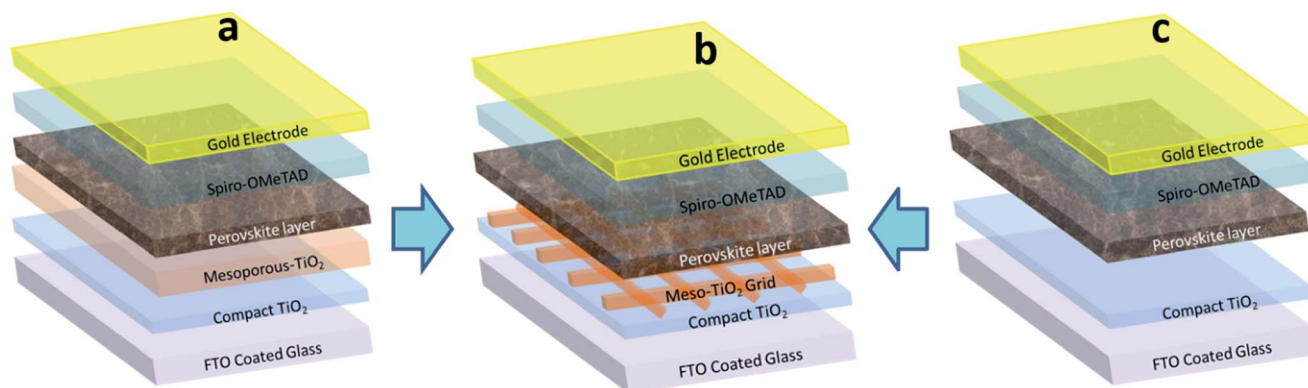

Fig. 1 Schematic diagram of (a) the mesoporous structure; (b) the meso–planar hybrid structure; and (c) the planar structure, of perovskite solar cells; the arrows are showing that the hybrid structure falls in between these two designs.

dark grey junction lines; the density of the junction decreases while moving from the grid perimeter to the center of the grid. This difference in coverage of the substrate with meso-TiO$_2$ results in the formation of hills and valleys repeatedly with the mesh size frequency, as can be clearly observed in Fig. 2d, which shows the cross sectional HR-SEM image of the TiO$_2$ grid assembled on the already deposited compact-TiO$_2$ layer on the glass substrate. As a result, we are able to obtain areas with and without meso-TiO$_2$, which are at regular intervals on the same substrate, forming the base for our meso–planar hybrid architecture of PSCs. The meso to planar ratio for the hybrid cells has been calculated from the covered area of the substrate with meso-titania, and has been found to be 1.08 (with 52% meso and 48% planar component in the cell). This means that the contribution of the mesoporous part in the cell is about half of the total area and hence should contribute in the performance of the cells. To see the effect of the meso to planar ratio on the device performance, the hybrid cells of grids with a larger mesh area *i.e.* 72 μm have also been fabricated. The meso to planar ratio was found to be 0.77 in this case (with 43.75% meso character and 56.25% planar character in the cell), as the areal contribution of the meso part is decreased. As a result, the cell is more close to the planar architecture due to the less contribution of meso-titania and the PV performance of the cells is expected to decrease in this case, as evident from the values in Table 1.

The cross section HR-SEM image of the meso–planar hybrid PSC is presented in Fig. 3, in which the junction between the planar area and the meso-area can be observed clearly. The MAPbI$_3$ based perovskite layer, which was directly deposited on the compact TiO$_2$ layer forming the planar part of the cell, can be seen on the left side (with pink color in the figure), which spreads over the meso-TiO$_2$ (with light orange color) on the right side of the image, forming the mesoporous part of the cell.

Photovoltaic performance of the solar cells

The photovoltaic performance of the best solar cells including the meso and planar cells as controls, is summarized in Table 1 and depicted in Fig. 4a. The average photovoltaic parameters are also presented in the table, evidencing the reproducibility of the results. Two different meshes with 50 and 72 micron mesh sizes were used to fabricate the meso-titania grid. This enabled the areal variation of the meso/planar ratio and was found to influence the performance of the cells drastically. It is clear
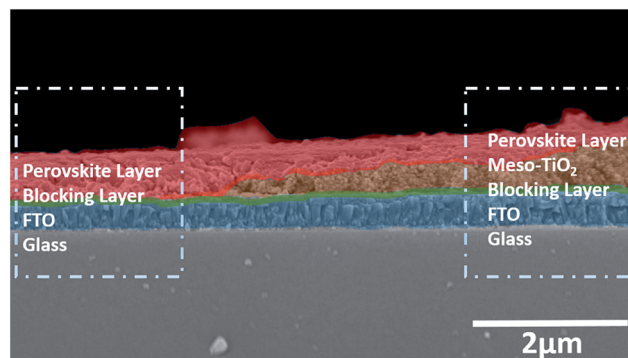

Fig. 3 Cross sectional HR-SEM image of the cell showing the planar part without meso-TiO$_2$, and the mesoporous part with TiO$_2$ can be clearly seen from the left to right part of the image (colors are used to distinguish only the layers, and the original SEM picture is provided in the ESI as Fig. S2†).

from the table that in the case of the smaller mesh size, *i.e.* 50 microns, the meso-contribution in the cell performance was dominating whereas in the case of the 72 micron grid, the planar contribution in the cell performance was found to be close to the planar architecture. It is evident from the table that all the photovoltaic parameters excluding the fill factor (FF) of the cells decrease while moving from meso to planar through meso–planar hybrid PSCs with increased planar behavior. Although higher V_{oc} of the planar cell was observed for the best cell fabricated, the average V_{oc} value follows a similar trend of decrease in these parameters with the increase in planarity. The fill factor on the other hand was 68.9% for the hybrid cells with a 50 micron grid sized cell, which is the best amongst all other solar cells. This can be attributed to the more efficient charge transportation in the presence of meso-titania even at a low content, as is also supported by the charge extraction measurements (discussed below).

Fig. 4a shows the *J*–*V* curves of representative cells with the different architectures. A better short circuit current density J_{sc} and open circuit voltage V_{oc}, reaching up to 20.28 mA cm^{-2} and 0.99 V, can be observed for the mesoporous PSC followed by the intermediate values for meso–planar hybrid cells and the least for planar cells. It is interesting to note here that even with the lower meso-character in our meso–planar hybrid cells with the 1.08 meso/planar ratio, we were able to conserve the current density, which indicates that the presence of meso-TiO$_2$ may not be an essential requirement to achieve high current in

Table 1 Photovoltaic performance of the best performing cells during the forward scan; the average values from the four cells of each type are provided in parenthesis. The standard deviation is also provided with the average performance in the parenthesis

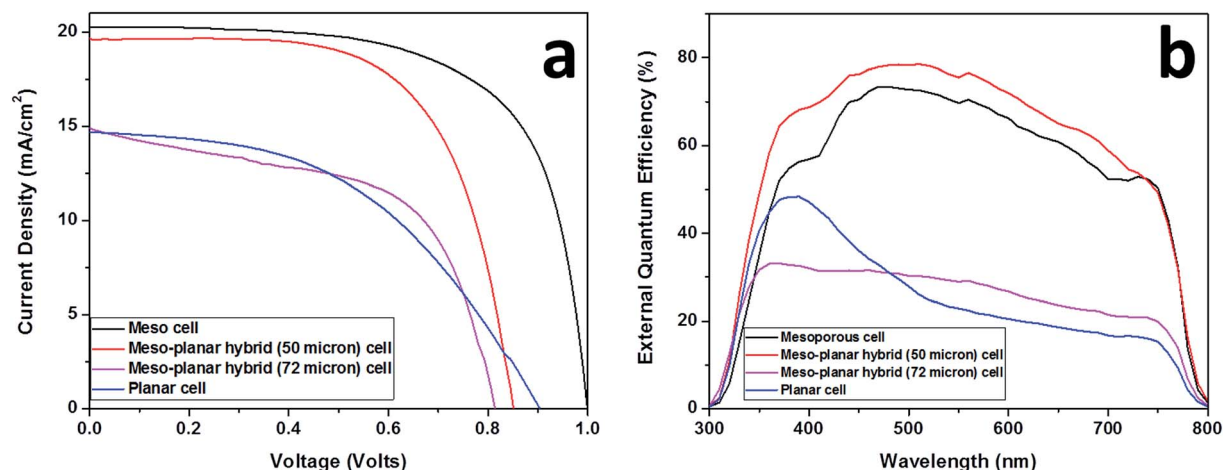| Cell architecture	J_{sc} (mA cm^{-2})	V_{oc} (V)	FF (%)	PCE (%)
Meso	20.28 (18.76 ± 1.36)	0.99 (0.98 ± 0.03)	66.0 (65.4 ± 2.9)	13.50 (12.08 ± 1.40)
Meso–planar hybrid (meso/planar = 1.08)	19.63 (18.05 ± 1.07)	0.86 (0.86 ± 0.01)	68.9 (68.2 ± 3.5)	10.76 (9.63 ± 0.66)
Meso–planar hybrid (meso/planar = 0.77)	14.99 (13.25 ± 1.55)	0.81 (0.80 ± 0.03)	56.9 (59.6 ± 1.8)	6.93 (6.35 ± 0.49)
Planar	14.67 (13.77 ± 2.37)	0.90 (0.81 ± 0.11)	47.4 (49.7 ± 2.1)	6.29 (5.39 ± 1.55)

Fig. 4   (a) $J–V$ characteristics of perovskite solar cells (PSCs) for the different architectures (please refer ESI Fig. S1a–d† for the extent of hysteresis during forward and backward scan), and (b) the comparative EQE curve for these cells.

perovskite solar cells; moreover the lower amount of meso-titania in these cells is sufficient to provide good charge transportation and hence high current density. The lower current density in planar cells, as can be seen in Fig. 4a, can be attributed to less photon absorption or to a difference in the thickness of the perovskite layer in the planar cells due to the absence of the meso-TiO$_2$ layer. This can be supported by the absorption spectra of meso and planar solar cells provided in Fig. S4.† It is evident from the figure that the planar cell has less absorption in the entire MAPbI$_3$ absorption range, due to the thinner perovskite layer. On the other hand, decrease in V_{oc} has been observed from the meso to meso–planar hybrid structure. This decrease in V_{oc} of meso–planar hybrid cells as compared to meso-cells can be attributed to the presence of recombination centers on the peaks (junctions) of meso-TiO$_2$ in the grid structure, where in these peaks the perovskite is absent or at low coverage due to the height of the TiO$_2$ grid as shown in Fig. S3.† These peaks are responsible for providing direct contact between the spiro and the meso-TiO$_2$, increasing the probability of recombination on these points and hence decreasing the V_{oc} in this architecture. Improvement in the square nature of the $J–V$ curve results in the highest fill factor among all these architectures. We expect that these cells may even perform better than meso-cells after improvement of perovskite coverage on less covered places, which we consider as recombination centers, shown in Fig. S3 in the ESI.†

All the cells were found to behave differently during forward and backward $J–V$ scans, i.e. from J_{sc} to V_{oc} and V_{oc} to J_{sc} respectively, resulting in the non-overlapping $J–V$ curves termed as hysteresis and can be seen in Fig. S1 of the ESI.† The hysteresis is most commonly observed in perovskite cells, prepared with the mesoporous architecture,[23] and can be overcome by using an organic ETL in planar cells.[14,15] We have observed different extents of hysteresis in different architectures. It was found to increase from meso to planar cells through hybrid meso–planar cells. This phenomenon may be explained on the basis of the structure of the cells: in the meso architecture, both the J_{sc} and V_{oc} have been found to be affected

by the direction of bias without changing the shape of the curve. On the other hand the current remains unaffected in the case of meso–planar hybrid cells with variation of the voltage and introduction of an 's' shape in the $J–V$ curve, indicating the charge accumulation during the backward scan in this architecture. Interestingly the 's' shape in the $J–V$ curve of the backward scan is pronounced in the case of the planar structure compared to the hybrid structure, which further supports that the meso–planar hybrid structure is an intermediate structure between meso and planar architectures.

The comparative External Quantum Efficiency (EQE) graphs for these cells are plotted in Fig. 4b. It is evident from the figure that better photon absorption and then charge collection in the entire MAPbI$_3$ absorption range for both the mesoporous and meso–planar hybrid cells take place, however the EQE is lower in the case of planar cells, especially while moving towards the red region of the spectrum. This may be further confirmed by the better match between the J_{sc} taken from the $J–V$ measurements and calculated by the integration of EQE values for both the meso and meso–planar hybrid architectures. The integrated value of the J_{sc} from EQE measurements is 17.1 mA cm^{-2}, in very good agreement with the 18.3 mA cm^{-2} observed in $J–V$ measurement of the meso–planar hybrid (50 micron with 1.08 meso/planar ratio) cell. The trend was followed by the meso-cells with a calculated J_{sc} value of 15.7 mA cm^{-2} compared to 19.1 mA cm^{-2} measured under the solar simulator through $J–V$ measurements. It is clear from the J_{sc} data in Table 1 that the meso–planar hybrid cell with the 0.77 meso to planar ratio behaves more like the planar cell, and the short circuit current density for both of them is almost equal, i.e. 14.99 and 14.67 for the meso–planar hybrid (72 micron grid) and planar, respectively. Hence the high degree of disagreement in current densities calculated from EQE data and taken from the $J–V$ scan has been observed in the case of planar cells as can be seen in Fig. 4b. No pretreatment was performed for any of the solar cell architectures, in particular, for the planar structure. A pretreatment in the planar configuration usually improves the agreement between the EQE and the solar simulator measurements.[24]
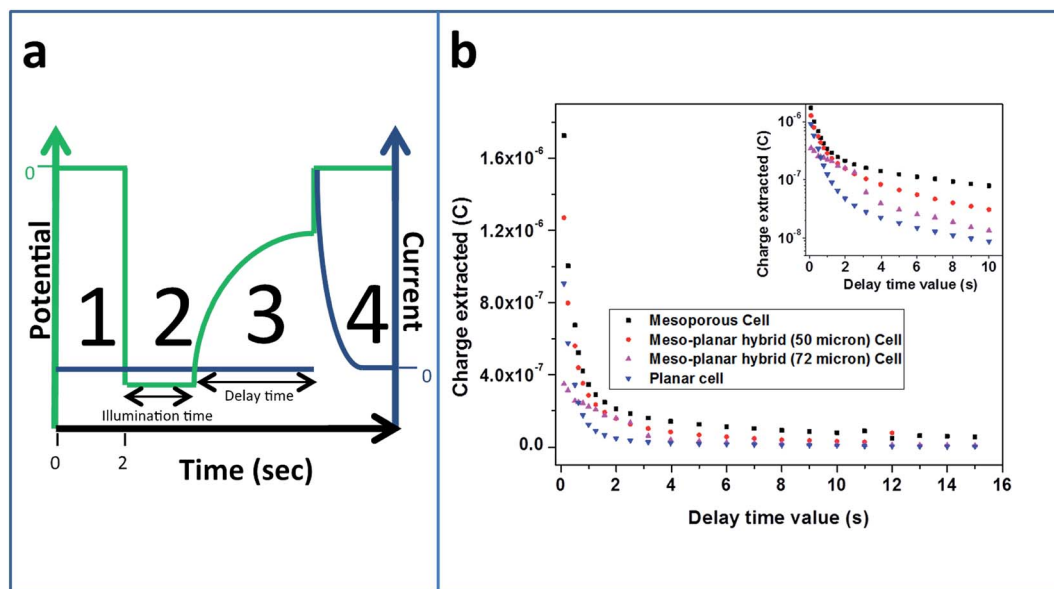
Fig. 5 (a) The steps involved in the charge extraction measurements. (b) Charge extraction of different types of cells using a white LED, inset is showing the semi-logarithmic graph of the charge extraction, presenting the difference between the cell structures.

Study of recombination behavior through charge extraction

The charge extraction method has been recognized as a well-established tool for studying electron transport and interfacial transfer in sensitized solar cells.[25] Fig. 5a shows the steps involved in the charge extraction (CE) measurement. (1) A two-second step in which the cell is being discharged in the dark; (2) the cell is then being disconnected and illuminated for 2 seconds (illumination time); (3) the light is then switched off and the system waits for a certain time called the delay time. In this step a charge recombination occurs inside the cell; (4) the cell is reconnected and the charges which were left and didn't recombine are extracted and measured. This process is being repeated for different delay times, from 0.5 seconds to 15 seconds.

Fig. 5b shows the charge extraction of the different cell architectures vs. increasing delay time. The amount of charge extracted is found to follow the order of the meso to meso–planar hybrid followed by planar cells. Looking at the CE graphs, it can be observed that in the case of the meso-structure based cells, more charges are left to extract for a certain delay time compared to the other architectures. This means that the rate of recombination in the meso-cells is lower than that for the other cell architectures. These results are in good agreement with the J–V curves (Fig. 4a), where the highest voltage has been obtained for mesoporous cells. The CE curves of the meso–planar hybrid cell (meso/planar ratio 1.08 with the 50 micron grid and meso/planar ratio 0.77 with the 72 micron grid) are located between the meso and the planar structures, which suggests that the rate of recombination in the hybrid cells is higher than that in the meso but lower than that in the planar structure. This can attributed to the high junctions of the TiO_2 grid which possess a direct contact between the TiO_2 and the spiro, resulting in recombination centers. High TiO_2 grid junctions can be observed in Fig. S3a–d.† These recombination

centers cause voltage loss for the hybrid architectures, as also supported by the J–V measurements. The semi-logarithmic plot of the CE curves in the inset of Fig. 5b clearly shows the closeness of these hybrid architectures with the mesoporous cells as compared to the planar structure.

Conclusions

In summary, a novel architecture, namely, meso–planar hybrid perovskite based solar cells, has been successfully fabricated and characterized for its photovoltaic performance and compared with the mesoporous and planar PSCs. The meso-planar hybrid cells were interestingly found to conserve the short circuit current density as compared to their meso-counterparts though some decrease in V_{oc} has been observed, which can be attributed to the complex structure of the cell with and without meso-TiO_2 at different places, resulting in two types of interfaces between the electron transporting layer and perovskite, specifically, ETL/perovskite (from the planar region) and ETL/meso-TiO_2/perovskite (in the meso-region) of the cell. The cells showed intermediate photovoltaic properties between the meso and planar architectures. The meso to planar ratio has been varied and the effect of the architecture on the photovoltaic parameters of the cells has been demonstrated. Charge extraction measurements reveal the recombination rate in these different cell architectures. The cells were successfully demonstrated to function as an intermediate between meso and planar structures and proved potentially important while studying the mechanisms of the PSCs.

Acknowledgements

Research Foundation under the CREATE program: Nano-materials for Energy and Energy-Water nexus.

Notes and references

1 A. Kojima, K. Teshima, Y. Shirai and T. Miyasaka, *J. Am. Chem. Soc.*, 2009, **131**, 6050–6051.

2 http://www.nrel.gov/ncpv/images/efficiency_chart.jpg.

3 M. Saliba, T. Matsui, J.-Y. Seo, K. Domanski, J.-P. Correa-Baena, M. K. Nazeeruddin, S. M. Zakeeruddin, W. Tress, A. Abate, A. Hagfeldt and M. Graetzel, *Energy Environ. Sci.*, 2016, **9**, 1989–1997.

4 M. A. Green, A. Ho-Baillie and H. J. Snaith, *Nat. Photonics*, 2014, **8**, 506–514.

5 S. Gamliel and L. Etgar, *RSC Adv.*, 2014, 29012–29021.

6 X. Xu, C. Randorn, P. Efstathiou and J. T. S. Irvine, *Nat. Mater.*, 2012, **11**, 595–598.

7 M. Saliba, S. Orlandi, T. Matsui, S. Aghazada, M. Cavazzini, J. P. Correa-Baena, P. Gao, R. Scopelliti, E. Mosconi, H. Dahmen, F. De Angelis, A. Abate, A. Hagfeldt, G. Pozzi, M. Graetzel and M. K. Nazeeruddin, *Nature Energy*, 2016, **1**, 15017.

8 G. Xing, N. Mathews, S. Sun, S. S. Lim, Y. M. Lam, M. Grätzel, S. Mhaisalkar and T. C. Sum, *Science*, 2013, **342**, 344–347.

9 S. D. Stranks, G. E. Eperon, G. Grancini, C. Menelaou, M. J. P. Alcocer, T. Leijtens, L. M. Herz, A. Petrozza and H. J. Snaith, *Science*, 2013, **342**, 341–344.

10 H. S. Kim, I. Mora-Sero, V. Gonzalez-Pedro, F. Fabregat-Santiago, E. J. Juarez-Perez, N. G. Park and J. Bisquert, *Nat. Commun.*, 2013, **4**, 2242.

11 F. Hou, Z. Su, F. Jin, X. Yan, L. Wang, H. Zhao, J. Zhu, B. Chu and W. Li, *Nanoscale*, 2015, **7**, 9427–9432.

12 T. C. Sum and N. Mathews, *Energy Environ. Sci.*, 2014, **7**, 2518–2534.

13 K. Wang, C. Liu, P. Du, J. Zheng and G. Xiong, *Energy Environ. Sci.*, 2015, **8**, 1245–1255.

14 M. Xiao, F. Huang, W. Huang, Y. Dkhissi, Y. Zhu, J. Etheridge, A. Gray-Weal, U. Bach, Y. B. Cheng and L. Spiccia, *Angew. Chem., Int. Ed.*, 2014, **53**, 9898–9903.

15 S. Ye, W. Sun, Y. Li, H. Peng, Z. Bian, Z. Liu and C. Huang, *Nano Lett.*, 2015, **15**, 3723–3728.

16 C. G. Wu, C. H. Chiang, Z. L. Tseng, M. K. Nazeeruddin, A. Hagfeldt and M. Graetzel, *Energy Environ. Sci.*, 2015, **8**, 2725–2733.

17 J. H. Heo, H. J. Han, D. Kim, T. K. Ahn and S. H. Im, *Energy Environ. Sci.*, 2015, **8**, 1602–1608.

18 S. S. Kim, S. Bae and W. H. Jo, *Chem. Commun.*, 2015, **51**, 17413–17416.

19 S. Aharon, M. Layani, B.-E. Cohen, E. Shukrun, S. Magadassi and L. Etgar, *Adv. Mater. Interfaces*, 2015, 1500118.

20 M. Layani and S. Magadassi, *J. Mater. Chem.*, 2011, **21**, 15378.

21 M. Layani, P. Darmawan, W. L. Foo, L. Liu, A. Kamyshny, D. Mandler and P. S. Lee, *Nanoscale*, 2014, **6**, 4572.

22 K. Higashitani, C. E. Mc Namee and M. Nakayama, *Langmuir*, 2011, **27**, 2080–2083.

23 N. J. Jeon, J. H. Noh, Y. C. Kim, W. S. Yang, S. Ryu and S. I. Seok, *Nat. Mater.*, 2014, **13**, 897–903.

24 C. Roldán-Carmona, O. Malinkiewicz, R. Betancur, G. Longo, C. Momblona, F. Jaramillo, L. Camacho and H. J. Bolink, *Energy Environ. Sci.*, 2014, **7**, 2968–2973.

25 N. W. Duffy, L. M. Peter, R. M. G. Rajpakshe and K. G. U. Wijayantha, *Electrochem. Commun.*, 2000, **2**, 658–662.